

Parametrized multiqubit gate design for neutral-atom based quantum platforms

Madhav Mohan,¹ Julius de Hond,² and Servaas Kokkelmans¹

¹*Department of Applied Physics and Eindhoven Hendrik Casimir Institute, Eindhoven University of Technology, P.O. Box 513, 5600 MB Eindhoven, the Netherlands*

²*PASQAL SAS, Fred. Roeskestraat 100, 1076 ED Amsterdam, The Netherlands*

(Dated: December 2, 2024)

A clever choice and design of gate sets can reduce the depth of a quantum circuit, and can improve the quality of the solution one obtains from a quantum algorithm. This is especially important for near-term quantum computers that suffer from various sources of error that propagate with the circuit depth. Parametrized gates in particular have found use in both near-term algorithms and circuit compilation. The one- and two-qubit versions of these gates have been demonstrated on various computing architectures. The neutral atom platform has the capability to implement native N -qubit gates (for $N \geq 2$). However, one needs to first find the control functions that implement these gates on the hardware. We study the numerical optimization of neural networks towards obtaining *families* of controls – laser pulses to excite an atom to Rydberg states – that implement phase gates with one and two controls, the C_1P and C_2P gates respectively, on neutral atom hardware. The pulses we obtain have a duration significantly shorter than the loss time scale, set by decay from the Rydberg state. Further, they do not require single-site addressability and are smooth. Hence, we expect our gates to have immediate benefits for quantum algorithms implemented on current neutral atom hardware.

I. INTRODUCTION

Quantum devices based on neutral atoms offer a unique approach to quantum information and computing. In these systems, individual atoms can be trapped in optical traps, called *tweezers*. Arrays with up to 6100 atoms [1] have been constructed – which demonstrates the promising scalability of the platform. Movement of trapped atoms in the array has also been demonstrated [2]. This is termed dynamic connectivity, and can be used to swap or entangle distant qubits in a grid. These features, combined with demonstrated two-qubit gate fidelities of $F = 0.997$ [3, 4], and error suppression using error correcting codes [5] make the platform competitive with other leading platforms such as superconducting circuits and trapped ion devices.

In neutral-atom architectures, quantum information is generally encoded in the low-lying electronic states of single atoms. Entanglement is mediated by exciting the atoms into high-lying electronic states – that is, states with a large principal quantum number n , termed *Rydberg states* – through lasers resonant with the desired transition. The interactions between such states are strong and long-ranged, and hence allow for the implementation of native multiqubit gates – that is, N -qubit gates with $N \geq 2$. Such gates have wide ranging applications in quantum error correction [6–8], quantum algorithms [9, 10] and quantum compilation [11, 12].

To implement these gates on hardware, however, one must devise pulses – that is, the time profile of the laser intensity and frequency – that can carry out the desired unitary transformation on the electronic states of the atoms. There exist both theoretical proposals, notably for k -qubit Toffoli and fan-out gates (for $k > 2$) [6, 13–16], as well as recent experimental demonstrations of these gates for the Rydberg platform [15, 17, 18]. No-

tably, Cao *et al.* implemented N -qubit rotation gates (for N up to 9) in order to generate cascaded GHZ states [17] by placing N atoms within interacting range of each other. The pulses devised to implement this gate are also *time-optimal* – meaning they are the shortest possible pulses that implement the corresponding unitary. Such pulses that implement the gate directly are significantly shorter in duration than implementing the decomposition of the gate in terms of one- and two-qubit gates [19], and are obtained numerically using a class of methods termed *quantum optimal control* (QOC) [13, 20].

Recent studies have also investigated the parametrized versions of such multiqubit gates – gates that implement some unitary $U(\phi)$, for M parameters $\phi = (\phi_1, \phi_2, \dots, \phi_M)$. In terms of variational algorithms, there are proposed applications of such gates towards simulating lattice gauge theories [21] and combinatorial optimization [22]. Further, for a given circuit, the inclusion of k -controlled phase, or C_kP gates (for $k \geq 2$) in the gate set can reduce the gate count and the total circuit evaluation time of the compiled circuit [12], thus reducing infidelities – as most error sources propagate in time [13]. This reduction is especially significant for the current era of quantum hardware, termed the noisy intermediate-scale quantum (NISQ) era. In these devices, the coherence times of the qubits are limited, and there are multiple sources of gate infidelity.

We investigate the problem of finding families of pulses that implement the C_1P and C_2P gates on Rydberg hardware. Employing numerical techniques from quantum optimal control, we find pulses for both gates that are fast – more specifically, the C_1P pulse we obtain is time-optimal, and the C_2P pulse operates on a time scale comparable to the time-optimal solution. These pulses are also smooth, and require only *global* addressing – the same pulse is sent to all atoms – and hence can be im-

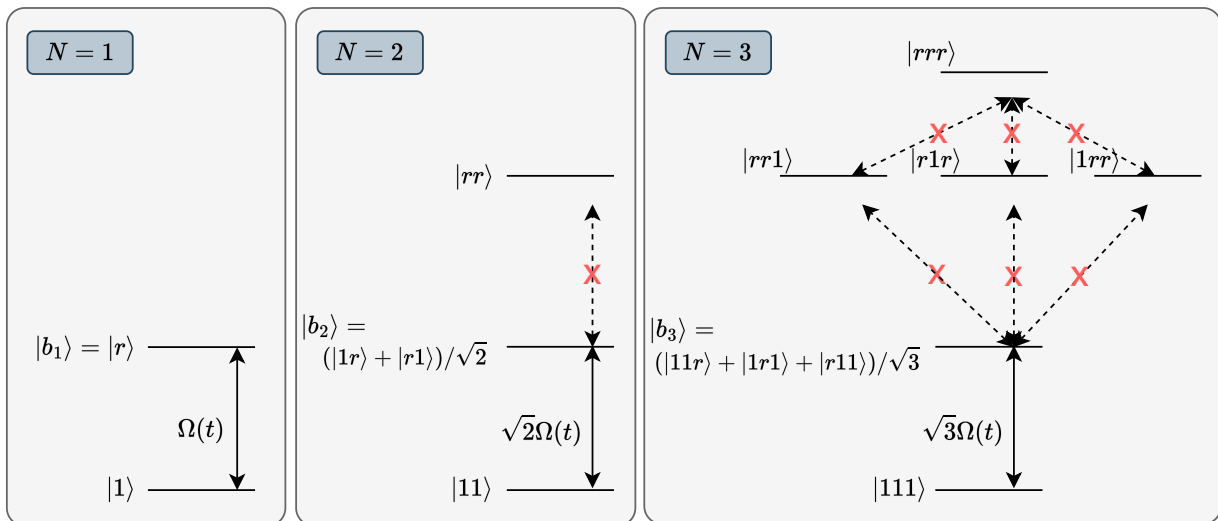


FIG. 1: Relevant level diagrams for the C_kP gate pulses. Of the computational basis states, only $|1\rangle$ is drawn since $|0\rangle$ is not coupled to $|r\rangle$. The left, middle, and right panels correspond to the one, two, and three-qubit case, respectively. Not all the levels involved are illustrated – for instance, $|110\rangle$ can be understood in terms of the $|11\rangle$ level for the two-qubit case. Due to the Rydberg interaction, higher excited states are detuned and are not coupled, as indicated by the red crosses.

plemented on NISQ devices.

We note that although preliminary work exists on C_1P gate protocols for the Rydberg platform (which we will discuss in Sec. II A), the C_2P protocol has not been explored to the best of our knowledge. Hence, our paper presents the first C_2P protocol for the Rydberg platform. Further, the techniques we use for the optimization can be extended to gates over more control qubits, as well as to fast quantum state preparation for parametrized states.

This work is structured as follows. In Section II we discuss the physics of our system – including the blockade mechanism by which entanglement is generated, as well as the dynamics of the quantum states when pulses are applied to the atoms. We also expand upon the optimization techniques we use to obtain the pulses. In Section III we present the results of the numerical optimization – the pulses we obtain – and study features of interest, including the gate time and sources of error. Finally, in Section IV we conclude by discussing future directions of research.

II. THEORY

A. Multiqubit gates

In the neutral atom architecture, we consider the *ground-ground* (gg) qubit scheme [23] – where quantum information is encoded in low-lying electronic states of neutral atoms. Such states are long lived and can allow for excellent coherence times of the qubits [24]. As an example we consider the strontium-88 (^{88}Sr) atom,

but note that the protocols we will obtain also work for other atoms – popular choices being ytterbium-141 [25] and rubidium-87 [15].

We encode $|0\rangle$ in the ground $5s^2\ ^1S_0$ state and $|1\rangle$ in the metastable $5s5p\ ^3P_0$ state. The Rydberg state $|r\rangle$ should have a large enough n such that strong interactions are generated – for instance, the $5s61s\ ^3S_1$ state was chosen by Tsai *et al.* in their demonstration of the current platform-leading two-qubit gate fidelities [3].

The problem we are concerned with is *family control* [19] – given a target unitary transformation $U_{\text{tgt}}(\phi)$ for parameters $\phi = (\phi_1, \phi_2, \dots, \phi_M)$, obtain the *family* of control pulses $\mathbf{C}(\phi, t)$ that implement the transformation for some control hamiltonian H_C , on quantum hardware. By family of pulses, we hence mean control functions that are continuous in ϕ . For a neutral atom device with N atoms, this family of controls includes the Rabi frequency

$$\mathbf{\Omega}(\phi, t) = (\Omega_1(\phi, t), \Omega_2(\phi, t), \dots, \Omega_N(\phi, t)), \quad (1)$$

and the detuning

$$\mathbf{\Delta}(\phi, t) = (\Delta_1(\phi, t), \Delta_2(\phi, t), \dots, \Delta_N(\phi, t)), \quad (2)$$

that are proportional to the laser intensity and laser frequency respectively. We note that the controls are vectors in the general case, as one could consider addressing each atom individually with a separate laser. Here $\Omega_i(t) \propto \sqrt{P_i}$ – for P_i the power of the i^{th} laser – and $\Delta_i(t) = (\omega_{L,i}(t) - \omega_{1,r})$, for $\omega_{L,i}(t)$ the frequency of the i^{th} laser. Hence,

$$\mathbf{C}(\phi, t) = (\mathbf{\Omega}(\phi, t), \mathbf{\Delta}(\phi, t)). \quad (3)$$

We aim to find hardware controls to implement, natively, the k -controlled phase gates [12] for $k = 1, 2$ –

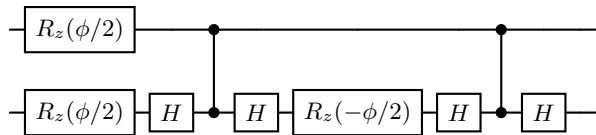


FIG. 2: The decomposition of a $C_1P(\phi)$ gate into the standard gate set of a Rydberg device requires two C_1Z gates and several single-qubit gates. It has a longer pulse duration, and hence more error-prone, than a *native* implementation of the C_1P gate which we present in Sec. III A.

corresponding to a two-qubit and three-qubit gate respectively.

The corresponding target unitaries are

$$U_{C_1P}(\phi) = |0\rangle\langle 0|_1 \otimes (\mathbb{1}^1)_2 + |1\rangle\langle 1| \otimes P(\phi)_2 \quad (4)$$

$$U_{C_2P}(\phi) = (\mathbb{1}^2 - |11\rangle\langle 11|)_{1,2} \otimes (\mathbb{1}^1)_3 + |11\rangle\langle 11|_{1,2} \otimes P(\phi)_3, \quad (5)$$

where the superscript on the identity $\mathbb{1}$ denotes the number of qubits it acts on, the subscript denotes the label of the qubit(s), and P is the *phase* gate

$$P(\phi) = \begin{bmatrix} 1 & 0 \\ 0 & e^{i\phi} \end{bmatrix}. \quad (6)$$

One can always implement such transformations by decomposing them into a product of one- and two-qubit gates available on the hardware – this is visualized for the C_1P gate in Fig. 2. However, this approach has a significantly longer gate duration [19, 26] than the control-level approach we adopt. In Appendix C, we present an in-depth comparison of these two approaches for our problem.

We note that as $P(\pi) = Z$, $C_kP(\pi)$ is equivalent to a C_kZ gate. Hence, the problem we consider is the generalized version of the problem of obtaining a C_kZ pulse [13, 27–29].

To illustrate the physics of the blockade gate, consider first the case where one applies a laser field near-resonant to the ground to Rydberg state transition (specifically, from $|1\rangle$ to $|r\rangle$), to a pair of atoms. The single-qubit Hamiltonian, then, is

$$H_{1q}(\Omega(t), \Delta(t)) = \frac{\Omega(t)}{2} (|1\rangle\langle r| + h.c.) - \Delta(t) |r\rangle\langle r|. \quad (7)$$

Note that we set $\hbar = 1$ throughout this article.

As the time-optimal C_kP pulses have constant laser intensity [29], we keep the Rabi frequency fixed to a constant in our optimization, $\Omega(t) = \Omega_{\max}$. We also enforce global pulses, that is, the same pulse is simultaneously applied to all atoms, and hence $\Delta_i(t) = \Delta(t)$. This simplifies the experiment considerably as only one laser is required to implement the gate, further, single site addressability – an experimental challenge [13, 30] – is not

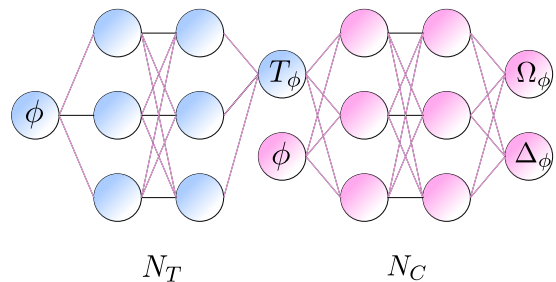


FIG. 3: We visualize two *chained* NNs, and label the input and output layers with the corresponding physical values. The intermediate layers consist of neurons with each edge representing a trainable weight in the weight matrices, \mathbf{W}_T and \mathbf{W}_C for N_T and N_C respectively. The neuron applies a weighted sum followed by an *activation function* – See Appendix A for details. This is an example of N_{TC} – the networks we use to find $C_{C_kP}(\phi, t)$ have Ω_ϕ fixed to a constant.

needed. The control function of Eq. (3) hence reduces to $C_{C_kP}(\phi, t) = \Delta(\phi, t)$.

For N atoms then, the physics is captured by the Hamiltonian

$$H_{Nq} = \sum_{i=1}^N H_{1q}^i(\Omega(t), \Delta(t)) \Big|_{\Omega(t)=\Omega_{\max}} + \sum_{i=1}^N \sum_{j>i}^N H_{\text{int}}^{i,j}, \quad (8)$$

where

$$H_{1q}^i = \mathbb{1}_1 \otimes \mathbb{1}_2 \otimes \dots \otimes (H_{1q})_i \otimes \dots \otimes \mathbb{1}_N, \quad (9)$$

and

$$H_{\text{int}}^{i,j} = -\frac{C_6}{|\mathbf{R}_i - \mathbf{R}_j|^6} (\mathbb{1}_1 \otimes \mathbb{1}_2 \otimes \dots \otimes |r\rangle\langle r|_i \otimes \dots \otimes |r\rangle\langle r|_j \otimes \dots \otimes \mathbb{1}_N). \quad (10)$$

Note that the indices i, j denote the atom(s) the operator acts on. Here, $H_{\text{int}}^{i,j}$ describes the van der Waals interaction between two atoms excited to the Rydberg state, with C_6 the van der Waals interaction coefficient and \mathbf{R}_k the displacement vector of the k^{th} atom. We will only investigate systems with atoms placed equidistant from each other. Defining the pair-interaction energy as $V_{\text{int}}^{i,j} = -C_6/|\mathbf{R}_i - \mathbf{R}_j|^6$, this implies that

$$V_{\text{int}}^{i,j} = V, \quad \forall (i, j) \in A \times A \quad (11)$$

for $A = \{1, 2, \dots, N\}$. We will refer to $B = V/\Omega_{\max}$ as the *blockade strength*. In this work we will assume that $B \gg 1$ – this is called the blockade regime, as the presence of one atom in the Rydberg state suppresses the Rydberg population of neighboring atoms [31].

For an N -qubit system in this regime that evolves under the Hamiltonian from Eq. (8), one can realize unitaries that map each computational basis state to itself up to a phase [29], which makes it well suited to realizing $C_{N-1}P$ gates [12] – upto a global single qubit R_Z rotation. The dynamics in the blockade regime can be

understood in terms of two-level systems (TLS): two and three for the C_1P and C_2P gate, respectively. We illustrate these systems in Fig. 1. The TLS are closed systems – independent of each other, they partition the Hilbert space into subspaces with populations that do not mix [29].

We consider first the C_1P gate, that acts on the computational space $\{|00\rangle, |01\rangle, |10\rangle, |11\rangle\}$, and is described by the matrix $U = \text{diag}(1, 1, 1, e^{i\phi})$ – this is equivalent to the unitary from Eq. (4). We note that H_{2q} does not act on $|00\rangle$, as H_{1q} does not act on $|0\rangle$. This implies that the dynamics of states $|01\rangle$ and $|10\rangle$ is equivalent, involving a transition $|1\rangle \leftrightarrow |r\rangle$ with coupling strength Ω_{\max} , forming the first TLS. The transfer from the $|11\rangle$ state to the $|rr\rangle$ state is forbidden for the case of a perfect blockade ($B \rightarrow \infty$) and this state forms the second TLS along with the two-qubit *bright* state

$$|b_2\rangle = \frac{1}{\sqrt{2}}(|1r\rangle + |r1\rangle), \quad (12)$$

which involves the transition $|11\rangle \leftrightarrow |b_2\rangle$ with Rabi frequency $\sqrt{2}\Omega_{\max}$ [29].

The C_2P gate is described by the matrix $U = \mathbb{1}^3 - 2e^{i\phi}|111\rangle\langle 111|$ – equivalent to the definition in Eq. (5). The dynamics involves the two TLS described above, along with a third TLS involving the transition $|111\rangle \leftrightarrow |b_3\rangle$ with the Rabi frequency $\sqrt{3}\Omega_{\max}$, where

$$|b_3\rangle = \frac{1}{\sqrt{3}}(|11r\rangle + |1r1\rangle + |r11\rangle) \quad (13)$$

is the three-qubit bright state.

Assuming perfect blockade $B \rightarrow \infty$, we can hence project out the forbidden states with more than one Rydberg excitation [13]. This leads to an effective Hamiltonian H_{eff} , defined in Eq. B2 for a three-qubit system.

We note, however, that the blockade strength is finite in the experiment [as computed in Eq. (10)], and this is a potential source of infidelity for gates optimized at $B \rightarrow \infty$. For the C_1P gate, we will hence simulate the dynamics (during the optimization) under the full Hamiltonian from Eq. (8) with $B = 21.1$ [27], an experimentally realistic value – as opposed to simulating H_{eff} . This is done in order to mitigate the finite blockade errors [28].

Motivated by reducing the computational expense for the higher-dimensional problem of the C_2P gate, we started by simulating the dynamics under H_{eff} instead. However, as we explore in Sec. III, this leads to pulses with high infidelities for finite B – and we used these solutions (optimized initially for H_{eff}) as initial guesses for a subsequent finite-blockade optimization.

B. Numerical optimization

Using established QOC techniques such as Gradient Ascent Pulse Engineering (GRAPE) [13, 32] or semi-analytical approaches [15, 29], one can obtain a pulse to

implement the C_kP gate for some fixed angle ϕ . Consider the use of C_kP gates in variational algorithms, where one might run the GRAPE algorithm to obtain the gate pulses, before carrying out the quantum circuit – such optimizations would need to be run after every iteration of the algorithm, as the gate angle ϕ is updated by a classical solver in each iteration [33]. This can lead to a significant overhead, considering that the runtime for GRAPE is longer than the runtime of the quantum circuit.

Sauvage *et al.* investigated the generation of parametrized gates by training neural networks (NNs) – used as *variational ansätze* – to model families of pulses [19]. We build upon their approach, and adapt it to our neutral atom system. As we will motivate in this section, compared to GRAPE, the NN only has to be trained once, and then outputs a high-fidelity pulse for any angle in the domain of the gate without requiring further optimizations.

NNs consist of multiple layers, each with a collection of nodes, called *neurons*, and trainable weights. In Appendix A, we discuss how these layers and neurons transform the inputs (in the form of vectors). NNs with the appropriate weights can approximate any continuous, multivariate function [34].

The inputs to the NN – which we call N_C – are ϕ and total pulse duration T_ϕ . The angle ϕ is sampled randomly from the domain, $\text{dom}(C_kP) : (0, \pi]$. The open interval is chosen as, for $\phi = 0$, $C_kP(0) = \mathbb{1}$ is equivalent to not implementing a pulse, and $T_{\phi=0} = 0$. We request $C_{C_kP}(\phi, t)$ from the NN as the output. Once the pulses are obtained from the NN, we evolve the system under the Hamiltonian in Eq. (8) to obtain the output unitary

$$U_{\text{out},k}(\phi) = \mathcal{T} \exp \left(-i \int_0^{T_\phi} H_{(k+1)q}(C_{C_kP}(\phi, t)) dt \right), \quad (14)$$

for \mathcal{T} the time-ordering operator. The cost function at each iteration is

$$J = 1 - \frac{1}{4^{(k+1)}} \langle \|U_{C_kP}(\phi)^\dagger (P U_{\text{out},k}(\phi) P)\|^2 \rangle_\phi \quad (15)$$

where P is the projection operator onto the computational subspace [35], $\|\cdot\|$ the Hilbert-Schmidt norm and $\langle \cdot \rangle_\phi$ implies we average over samples of ϕ drawn randomly from $\text{dom}(C_kP)$ in each iteration. We will refer to $J = \langle (1 - F) \rangle_\phi$ as the average *infidelity* over the domain of the protocol. We then train the weights of the NN to minimize the cost function.

We first look at how the optimization works when the total pulse duration is fixed to some constant for each angle, $T_\phi = T$:

1. Initialize the weights \mathbf{W}_C of N_C randomly.
2. Construct a vector \mathbf{v}_{in} with M angles drawn randomly from $\text{dom}(C_kP)$, we fixed $M = 80$. Input \mathbf{v}_{in} to the network N_C .

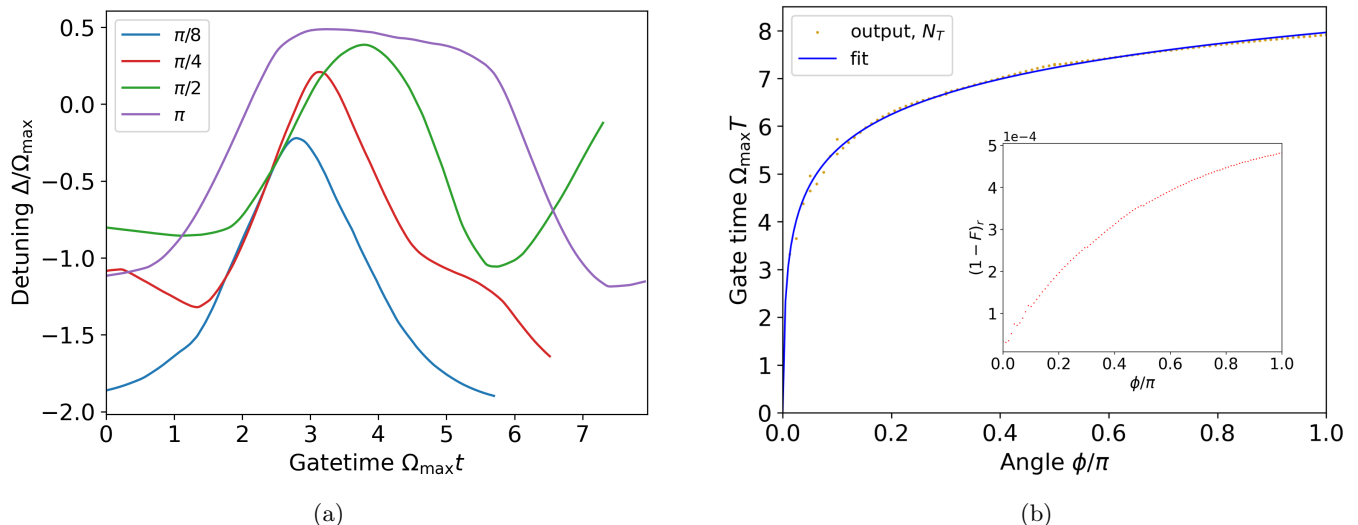


FIG. 4: (a) Laser detuning Δ that implements, for different angles $\phi \in (0, \pi]$, the time-optimal C_1P gate. The laser intensity is kept fixed at the maximum value for the time-optimal pulses, such that the Rabi frequency $\Omega = \Omega_{\max}$. (b) The pulse time as a function of ϕ [NN output, fit to Eq. (17)]. Inset: We plot $(1 - F)_r$ – the infidelity arising due to decay from $|r\rangle$, as a function of ϕ .

3. The network outputs $C_{C_kP}(\mathbf{v}_{\text{in}}, t)$ by carrying out transformations on \mathbf{v}_{in} as in Eq. (A1). We get a vector of control pulses as the output, one for each angle in \mathbf{v}_{in} .
4. Compute J by evolving the system as in Eq. (14) with $T_\phi = T$, and computing the distance between the output unitary and the target unitaries from Eq. (4) and (5).
5. Compute the gradients $\nabla_{\mathbf{W}_C} J$ i.e. the gradient of the cost function with respect to each weight.
6. Use an optimizer (e.g. Adam [36]) that updates the weights $\mathbf{W}'_C = \mathbf{W}_C + \delta\mathbf{W}_C$ based on $\nabla_{\mathbf{W}_C} J$.
7. Perform steps 2 to 6 in a loop until convergence is reached (as determined by a pre-selected convergence criterion).

In general, however, the total pulse duration is a function of ϕ [29]. Further, physical errors – arising from Doppler shifts due to the finite temperature of atoms, or decay from $|r\rangle$ – propagate in time, and it is hence desirable to minimize the pulse duration.

This can be included in our framework by adding a second NN: $N_T(\phi)$, with input ϕ and output T_ϕ . We chain N_T and N_C such that the output of N_T is input into N_C , and denote this chained network by N_{TC} – see Fig. 3 for an example. To minimize the duration, the cost function is modified appropriately,

$$J_{\text{opt}} = J + \mu T_\phi, \quad (16)$$

for a multiplier constant μ that is selected in a heuristic manner, and the rest of the optimization proceeds as discussed above: with \mathbf{v}_{in} now input to N_T .

As part of the steps outlined above, we must compute the gradient with respect to the NN weights $\mathbf{J}'_{\text{opt}} = \nabla_{\mathbf{W}_C} J_{\text{opt}}$. The numerical solver of the Schrödinger equation can itself be interpreted as a NN, where the depth of the network is a continuous variable – these are termed neural ODEs [19, 37]. This identification allows us to backpropagate [38] the cost function through the ODE solver: starting from J_{opt} we can repeatedly apply the chain rule backwards, first through the neural ODE, then the layers of N_{TC} , in order to compute \mathbf{J}'_{opt} [37, 39]. As the method is not specific to the Hamiltonian of the system, it is also generalizable to various quantum systems [19].

Randomly drawing \mathbf{v}_{in} in each iteration ensures that J_{opt} is evaluated over target angles previously unseen by the optimizer – this ensures that N_{TC} , once converged, will return a high-fidelity pulse for all values of ϕ .

In practice, we find that splitting $\text{dom}(C_kP)$ into multiple intervals and using a separate network N_{TC} for each such interval leads to better solutions – as quantified by a lower value for J_{opt} . This results in control functions piecewise continuous in ϕ . Operationally, these functions retain the advantage of the single N_{TC} approach – that outputs controls continuous in ϕ – over standard QOC techniques. That is, they need to be trained only once to output high-fidelity pulses for any $\phi \in \text{dom}(C_kP)$. Discussion of the justification and implications of this approach can be found in Appendix A.

As an alternative approach, one could use QOC techniques like GRAPE to compute the pulse for multiple input angles in the domain, and interpolate between them to obtain a solution continuous in ϕ – however, this interpolation step can introduce additional infidelities, and it fails if the pulses found at different angles belong to dif-

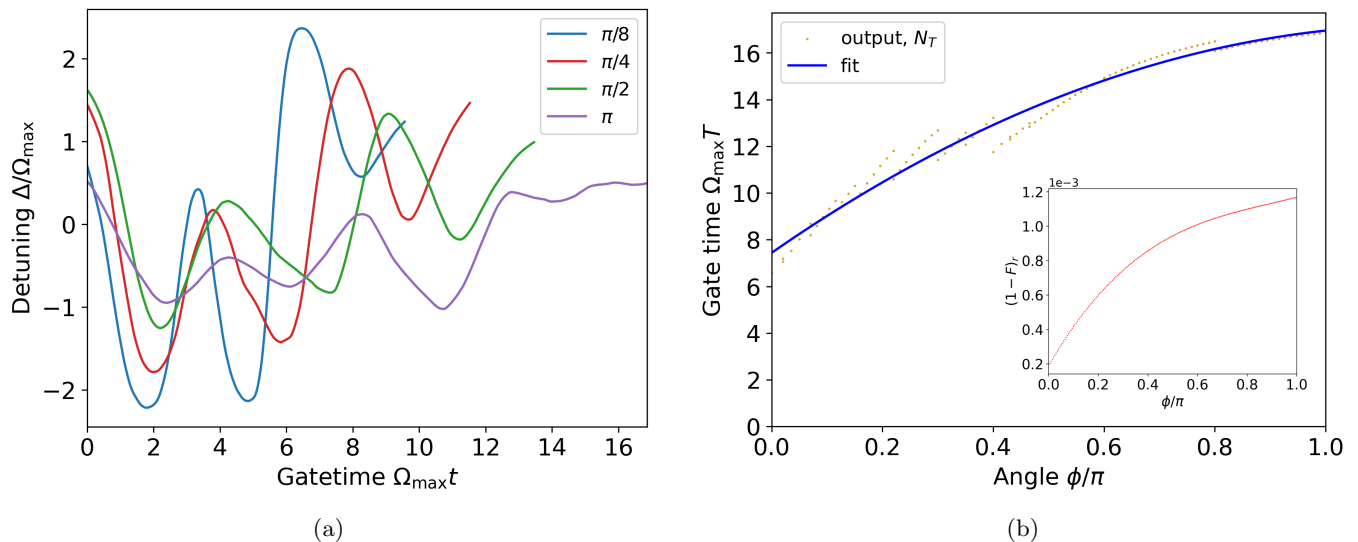


FIG. 5: (a) Laser detuning Δ to implement the C_2P gate. (b) The C_2P pulse time (NN output, fit to second-order polynomial) as a function of ϕ and (inset) the infidelity arising from Rydberg state decay.

ferent families [19, 40]. We note recent work that adapts this interpolation approach to mitigate the associated infidelities [41].

III. RESULTS

To compute the infidelity of our pulses in a realistic experimental setup, we simulate decay from the Rydberg state, with estimated lifetime $\tau = 96.5 \mu\text{s} (\simeq 6 \times 10^3 / \Omega_{\max})$ for the $n = 61$ state [28], considering a Rabi frequency of $\Omega_{\max} = 2\pi \times 10\text{MHz}$ for Sr, which is within reach in the near term [3, 27].

As discussed in Sec. II A, we also consider a realistic blockade strength of $B = 21.1$ [27], unless specified otherwise. Calculations of infidelities arising from the decay of $|r\rangle$, and from finite blockade, are discussed in Appendix B. The total mean infidelity $\langle(1-F)\rangle_\phi$ was computed over 100 samples randomly drawn from $\text{dom}(C_kP)$.

As a consequence of using multiple networks for each gate, T_ϕ – the output of N_T – is piecewise continuous in ϕ . We will, however, fit the output of N_T to continuous functions, in order to visualize and highlight the behavior of T_ϕ . The fit constants were determined by a non-linear least squares approach.

The detuning range of the pulses is constrained to $|\Delta(t)| < 2.5\Omega_{\max}$, as this simplifies the experimental implementation [28]. See Appendix A for details about the constraint implementation. The optimized NNs are included as additional data [42], and can be used to access the pulses for arbitrary ϕ .

A. C_1P gate

Simulating the errors as discussed above, we obtain a mean infidelity $\langle(1-F)\rangle_\phi = 3.4 \times 10^{-4}$ for the two-qubit C_1P gate over $\text{dom}(C_1P)$ – with the main error arising due to Rydberg state decay (see inset of Fig. 4b).

The pulses for some sample angles are plotted in Fig. 4, along with T_ϕ as a function of ϕ . We observe that the output from N_T agrees closely with a fit to the function

$$f(\phi) = a \operatorname{arcsinh}(b\phi), \quad (17)$$

for constants a, b , which is plotted in Fig. 4b. This plot is consistent with currently known results for time-optimal C_1P pulses [15, 29]. We consider finite B in our optimization, compared to $B \rightarrow \infty$ in the above studies, leading to minor differences ($\sim 2\%$ averaged over $\text{dom}(C_1P)$) in pulse duration.

Here, we also plot the infidelities arising due to decay from $|r\rangle$ – this indicates that not only T_ϕ , but the total time spent in the Rydberg state also increases with ϕ .

B. C_2P gate

We plot pulses for the C_2P gate, and the time-output of N_T fit to a second-order polynomial, in Fig. 5.

Considering only decay from the Rydberg state, we obtain an infidelity of $\langle(1-F)\rangle_\phi = 9.4 \times 10^{-4}$. Including finite B , this jumps drastically to $\langle(1-F)\rangle_\phi = 1.54 \times 10^{-2}$, thus rendering our pulses ineffective for the system we simulate.

The error arising from finite blockade is well studied for two-qubit gates, and protocols often preserve a high fidelity despite such errors [30, 43, 44]. The three-qubit

gates we obtain, however, have a greater pulse duration, and hence a lower fidelity for a finite B .

We hence study the strategy of using the C_2P NNs we trained at $B \rightarrow \infty$, as *initial guesses* for C_2P NNs trained at $B = 21.1$, and then re-run the optimization as discussed in Sec. II B. The pulses we obtain from this optimization reduce the average finite blockade infidelity to $\langle(1 - F)_{\text{int}}\rangle_\phi = 4 \times 10^{-4}$, and the total infidelity $\langle(1 - F)\rangle_\phi = 1.2 \times 10^{-3}$ – where the decay from the Rydberg state is the main source of infidelity. The results of this optimization are visualized in Fig. 6, in Appendix B.

We note that we have to divide the domain in more steps and that hence more networks are needed than for the C_1P protocol – 14, compared to 5 – and the network architecture is more complex. This leads to more pronounced discontinuities in T_ϕ with respect to ϕ for the C_1P pulses – see Appendix A.

Our approach hence converges to a high-fidelity solution, but not the time-optimal one (for which T_ϕ would be continuous in ϕ , or agree closely with a continuous function as in Sec. III A). However, the pulse operates on a time scale comparable to the time-optimal solution – the $C_2P(\pi)$ pulse, for instance, has a duration of $T_\pi = 16.87/\Omega_{\text{max}}$, which is around 2.6% higher than the time-optimal C_2Z pulse [13].

IV. CONCLUSION

In this work we presented families of pulses that implement C_1P and C_2P gates on the neutral atom hardware with a high fidelity, in the presence of experimental sources of infidelity. Further, the NN weights we found could be valuable initial guesses for further optimizations – for instance, to find pulses robust to hardware-specific sources of error like laser intensity noise [28].

It is of interest to extend these techniques for a larger number of control qubits, that is, C_kP gates for $k > 2$. NNs with a more complex architecture would be needed for such optimizations, and training such NNs without encountering vanishing gradients, or large runtimes, would benefit from additional machine learning techniques like regularization and batch normalization [45]. The Hilbert space dimension $d = 3^{k+1}$ scales exponentially with the number of qubits, and will limit the k achievable on a classical computer. However, we expect the training of NNs using graphics processing unit (GPU) clusters [46], along with tensor network based methods for the simulation of the dynamics [47, 48] to enable us to find controls for larger values of k .

We note that a shorter version of the C_2Z gate – exploiting an alternative definition of the C_2Z unitary – has been proposed [15], and an associated family of C_2P pulses may also be investigated. The corresponding optimization, however, requires an arbitrary global single-qubit rotation $U_1(\phi)$ instead of a correctional R_Z rotation that one appends to the pulses, to implement the

C_kP unitary [27]. This adds three functions (the rotation angles) to be optimized for, and is computationally expensive.

DATA AVAILABILITY

The weights for the NNs presented above, the parameters to specify their architecture (introduced in Appendix A), and a tutorial are included as additional data [42]. The code used for training the NNs is available upon reasonable request.

ACKNOWLEDGEMENTS

We acknowledge valuable discussions with Lucas Leclerc, Sven Jandura and Raul dos Santos. We note the use of the libraries PyTorch [49] and torchdiffeq [50] for carrying out the NN-based optimization.

This research has received funding from the European Union’s Horizon 2020 research and innovation programme via the project 101070144 (EuRyQa) and under the Marie Skłodowska-Curie grant agreement number 955479. S.K. acknowledges funding from the Dutch Ministry of Economic Affairs and Climate Policy (EZK) as part of the Quantum Delta NL programme, and from the Netherlands Organisation for Scientific Research (NWO) under Grant No. 680.92.18.05.

Appendix A: NN architecture and training

Consider a feedforward NN consisting of m_L layers, each with m_N neurons (with the exception of the input and output layers) – we visualized two such networks in Fig. 3, both with $(m_L, m_N) = (4, 3)$. We denote the weights in each layer l by \mathbf{W}_l – each weight is represented by an edge in Fig. 3, and hence \mathbf{W}_l is a matrix. The network N_T and N_C in Fig. 3, for instance, consist of 4 layers with 3 neurons in each intermediate, or *hidden*, layer.

Each neuron itself represents a weighted sum of the inputs (along with a *bias term* \mathbf{b}_l), as well as an *activation function*. The output from the n^{th} layer is

$$\mathbf{x}_n = f(\mathbf{W}_n \mathbf{x}_{n-1} + \mathbf{b}_n), \quad (\text{A1})$$

for *activation function* f that introduces non-linearities into the network. We use *fully connected* NNs in our research – where a neuron in a layer k is connected, by an edge, to every neuron in layer $k + 1$.

We choose the sigmoid activation function $f_\sigma(y) = 1/(1 + e^{-y})$ for the output layers, as the output can be conveniently bounded to some desired value – we bound $|\Delta(t)| < 2.5\Omega_{\text{max}}$ to make the pulse implementation more feasible on current generation hardware. We bound $T_\phi < 1.2T_{\text{opt}, \phi=\pi}$, i.e. by the

optimal time for the C_1Z and C_2Z gates, which are known [13] – slightly higher than $T_{\text{opt},\phi=\pi}$ as we wish to avoid vanishing gradients which arise for $f_\sigma \simeq 1$. This restricts the solution space and hence aids convergence to the true solution. We choose the *rectified linear unit* (ReLU) activation function for the intermediate layers, $f_{\text{ReLU}}(x) = \max(0, x)$.

The NN architecture for N_{TC} is determined by the choice of the activation function, and by $(m_L^T, m_N^T, m_L^C, m_N^C)$ – the layers and intermediate layer neurons for N_T and N_C respectively. The deeper and wider the network (the larger the m_L and m_N respectively), the larger the variational space – hence the higher the likelihood that the true solution lies in the space. However, this complexity can also make it difficult to train the network – such large NNs have the tendency to suffer from vanishing gradients [51].

A balance must hence be struck when choosing m_L and m_N to account for both the above factors – we note for instance that the optimization for the C_2P pulses is more challenging than for C_1P , owing in part to the larger dimension of the Hamiltonian (27×27 as opposed to 9×9), more phases (picked up by the different computational states) to account for [13], and a longer pulse time.

We choose these parameters in a heuristic manner. In principle, one N_{TC} with the appropriate architecture should be able to model the pulses over $\text{dom}(C_kP)$. As discussed above, however, finding this architecture is a challenge. On using deep NNs, we often encountered vanishing gradients that slow down convergence – this occurs for $m_L^C > 20, m_N^C > 300$, the parameters for N_C .

As presented in the main text, an alternative approach is to use NNs with fewer layers and weights, that can accurately model the pulses over a part of the $\text{dom}(C_kP)$. We then split this domain into multiple parts and assign one NN to be trained for each part.

For the C_1P NNs we used the architecture (3, 45, 10, 300), and for the C_2P NNs (4, 45, 20, 300).

This approach could potentially allow for multiple families of pulses to be found. Operationally, however, this does not make a difference compared to using one N_{TC} – both approaches return pulses that implement the desired gates over the entire domain. Further, we use the converged NN trained over one part of $\text{dom}(C_kP)$ as the initial guess for all other parts, to speed up convergence – this also reduces the likelihood of obtaining a separate pulse family.

Using the multiple N_{TC} approach also implies that discontinuities might arise in T_ϕ at the *junction points* of the domain parts – that is, T_ϕ is piecewise continuous instead of continuous. For the C_1P these discontinuities are minor and we obtain a good fit for T_ϕ with Eq. (17), and with results from other studies [15, 29], as discussed in the main text. For the C_2P optimization these discontinuities are more significant, partly because more N_{TC} were needed – 14 as opposed to 5 for C_1P – introducing more junction points.

The constants for the function in Eq. (17), determined

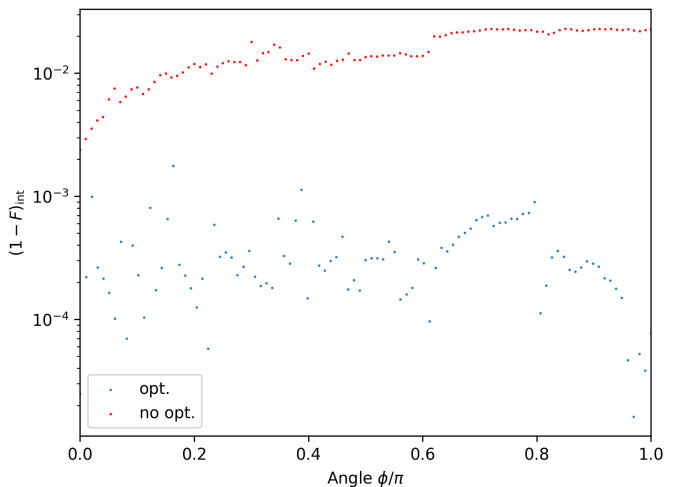


FIG. 6: Infidelities arising from finite blockade strengths for unoptimized *infinite blockade* pulses (red) and optimized pulses (blue). Our method is successfully able to mitigate the blockade-induced losses.

by fitting to the output of N_T for the C_1P protocol are $(a, b) = (1.07, 275.86)$. Similarly, the constants for the second-order polynomial $f(x) = ax^2 + bx + c$ for the C_2P protocol are $(a, b, c) = (-0.70, 5.24, 7.44)$.

Appendix B: Losses from finite blockade and Rydberg state decay

As discussed in Sec. II A, the assumption of blockade strength $B \rightarrow \infty$ implies that states with more than one Rydberg excitation cannot be populated during the pulse. This allows us to project them out by defining an effective Hamiltonian H_{eff} , in order to reduce the computational cost of the simulation, with the potential downside of added infidelities in a realistic system (with finite B), as we explored in Sec. III B.

First, for some operator G , we define $P_\Sigma(G)$ as an operator constructed from the sum over *distinct permutations* of qubit states, for instance,

$$P_\Sigma(|011\rangle) (\langle 0|_1 \otimes \langle b_2|_{2,3}) = |011\rangle (\langle 0|_1 \otimes \langle b_2|_{2,3}) + |101\rangle (\langle 0|_2 \otimes \langle b_2|_{1,3}) + |110\rangle (\langle 0|_3 \otimes \langle b_2|_{1,2}). \quad (\text{B1})$$

For the C_2P protocol over three qubits, the Hamiltonian in the limit $B \rightarrow \infty$ is:

$$H_{\text{eff}} = \left[\frac{\Omega(t)}{2} P_\Sigma(|001\rangle) \langle 00r| + \frac{\sqrt{2}\Omega(t)}{2} P_\Sigma(|011\rangle) (\langle 0|_1 \otimes \langle b_2|_{2,3}) + \frac{\sqrt{3}\Omega(t)}{2} |111\rangle \langle b_3| - \Delta(t) \sum_{i,j \in \{0,1\}} P_\Sigma(|ijr\rangle) \langle ijr| \right] + h.c. \quad (\text{B2})$$

To simulate the effects of spontaneous emission and blackbody radiation (BBR) at 300K from the Rydberg state, we add a non-Hermitian term [27, 28]

$$H_{\text{decay}} = i \frac{\Gamma_{n=61}}{2} |r\rangle \langle r|, \quad (\text{B3})$$

to H_{1q} in Eq. (7), which assumes that all decay occurs to states outside of the computational subspace – an assumption justified for the system we studied in this article [27, 52]. This term is subsequently used to construct the full Hamiltonian $H_{Nq,\Gamma}$, in a manner similar to Eq. (8). Here $\Gamma_{n=61}$ is the decay width of the $5s61s^3S_1$ state in Sr, corresponding to a lifetime $1/\Gamma_{n=61} = 96.5\mu\text{s}$ [28].

The infidelity due to decay from $|r\rangle$ was defined as

$$(1 - F)_r = F - F_{\text{decay}}, \quad (\text{B4})$$

for F, F_{decay} the fidelities are obtained by simulating the pulses under H_{Nq} [see Eq. (8)], and $H_{Nq,\Gamma}$ respectively. The infidelity arising from finite blockade was defined for three qubits, in a manner similar to Eq. (B4), $(1 - F)_{\text{int}} = F_{\infty} - F_{\text{fin}}$, for $F_{\infty}, F_{\text{fin}}$ the fidelities of the pulses simulated for H_{eff} and H_{3q} respectively. This infidelity is visualized as a function of ϕ for in Fig. 6.

We expect that the pulses optimized for some constant B will not retain a high fidelity for $B \rightarrow \infty$, or for some B' that differs significantly from the value considered. To obtain pulses that have a high fidelity at B' , the optimization has to be carried out again – the NN weights provided in the additional data serve as good initial guesses for this optimization.

Appendix C: Decomposition and native gates

As discussed in Sec. IIA, it is possible to implement the C_kP unitary by expressing it as a product of

hardware-available gate unitaries – we term this a decomposition based approach. An example of this approach, expressing the C_1P unitary in terms of single-qubit gates and the C_1Z gate, was presented in Fig. 2. The native approach, which we looked at, implements the C_kP unitary directly on the pulse level – that is, it is implemented by the dynamics induced by the laser pulses on the electronic states of the atoms.

It is worth comparing these two approaches for NISQ-era quantum computers. Qualitatively, finding optimal decompositions is a difficult problem, and it is complicated further if we include C_kZ gates in the standard gate set, as is the case for neutral atoms. We hence consider decompositions of the unitaries in terms of one- and two-qubit gates.

Let us define $T_{d,k}$ as the total time taken to implement two-qubit gates in the decomposition approach for C_kP , and $T_{n,k}$ as the time the native approach takes, averaged across the domain. We then propose the ratio $R_k = T_{d,k}/T_{n,k}$ as a metric for comparison. As one-qubit gates can be implemented with significantly higher fidelities [4, 53], we do not include them in $T_{d,k}$.

For the C_1P unitary, using the decomposition of Fig. 2 and time-optimal C_1Z gates [13], we obtain $R_1 = 2.2$. The C_2P gate can be decomposed into a product of two CNOT gates and three C_1P gates [54], which is equivalent to 8 C_1Z gates, and $R_2 = 4.6$. It is expected that R_k increases with k [19].

We note that this metric will differ depending on the decomposition scheme – it would be of interest to devise such schemes that account for the availability of C_kZ gates in the standard gate set.

-
- [1] H. J. Manetsch, G. Nomura, E. Bataille, K. H. Leung, X. Lv, and M. Endres, A tweezer array with 6100 highly coherent atomic qubits (2024), arXiv:2403.12021.
 - [2] D. Bluvstein, H. Levine, G. Semeghini, T. T. Wang, S. Ebadi, M. Kalinowski, A. Keesling, N. Maskara, H. Pichler, M. Greiner, *et al.*, A quantum processor based on coherent transport of entangled atom arrays, *Nature* **604**, 451–456 (2022).
 - [3] R. B.-S. Tsai, X. Sun, A. L. Shaw, R. Finkelstein, and M. Endres, Benchmarking and linear response modeling of high-fidelity Rydberg gates (2024), arXiv:2407.20184.
 - [4] A. G. Radnaev, W. C. Chung, D. C. Cole, D. Mason, T. G. Ballance, M. J. Bedalov, D. A. Belknap, M. R. Berman, M. Blakely, I. L. Bloomfield, *et al.*, A universal neutral-atom quantum computer with individual optical addressing and non-destructive readout (2024), arXiv:2408.08288.
 - [5] D. Bluvstein, S. J. Evered, A. A. Geim, S. H. Li, H. Zhou, T. Manovitz, S. Ebadi, M. Cain, M. Kalinowski, Hangleiter, *et al.*, Logical quantum processor based on reconfigurable atom arrays, *Nature* **626**, 58–65 (2023).
 - [6] S. E. Rasmussen, K. Groenland, R. Gerritsma, K. Schoutens, and N. T. Zinner, Single-step implementation of high-fidelity n -bit Toffoli gates, *Phys. Rev. A* **101**, 022308 (2020).
 - [7] D. Crow, R. Joynt, and M. Saffman, Improved Error Thresholds for Measurement-Free Error Correction, *Phys. Rev. Lett.* **117**, 130503 (2016).
 - [8] M. A. Perlin, V. N. Premakumar, J. Wang, M. Saffman, and R. Joynt, Fault-tolerant measurement-free quantum error correction with multiqubit gates, *Phys. Rev. A* **108**, 062426 (2023).
 - [9] K. Mølmer, L. Isenhower, and M. Saffman, Efficient Grover search with Rydberg blockade, *J. Phys. B* **44**, 184016 (2011).
 - [10] R. J. P. T. de Keijzer, V. E. Colussi, B. Škorić, and S. J. J. M. F. Kokkelmans, Optimization of the variational quantum eigensolver for quantum chemistry applications,

- AVS Quantum Sci. **4** (2022).
- [11] T. Patel, D. Silver, and D. Tiwari, Geyser: a compilation framework for quantum computing with neutral atoms, in *Proc. 49th Annu. Int. Symp. Comput. Arch.* (ACM, New York, 2022) p. 383–395.
- [12] K. Staudacher, L. Schmid, J. Zeiher, R. Wille, and D. Krausz, Multi-controlled Phase Gate Synthesis with ZX-calculus applied to Neutral Atom Hardware, *Electron. Proc. Theor. Comput. Sci.* **406**, 96–116 (2024).
- [13] S. Jandura and G. Pupillo, Time-Optimal Two- and Three-Qubit Gates for Rydberg Atoms, *Quantum* **6**, 712 (2022).
- [14] M. Khazali and K. Mølmer, Fast Multiqubit Gates by Adiabatic Evolution in Interacting Excited-State Manifolds of Rydberg Atoms and Superconducting Circuits, *Phys. Rev. X* **10**, 021054 (2020).
- [15] S. J. Evered, D. Bluvstein, M. Kalinowski, S. Ebadi, T. Manovitz, H. Zhou, S. H. Li, A. A. Geim, T. T. Wang, N. Maskara, *et al.*, High-fidelity parallel entangling gates on a neutral-atom quantum computer, *Nature* **622**, 268–272 (2023).
- [16] L. Isenhower, M. Saffman, and K. Mølmer, Multibit C_k NOT quantum gates via Rydberg blockade, *Quantum Inf. Process.* **10**, 755 (2011).
- [17] A. Cao, W. J. Eckner, T. Lukin Yelin, A. W. Young, S. Jandura, L. Yan, K. Kim, G. Pupillo, J. Ye, N. D. O’Connell, and A. M. Kaufman, Multi-qubit gates and Schrödinger cat states in an optical clock, *Nature* **634**, 315 (2024).
- [18] H. Levine, A. Keesling, G. Semeghini, A. Omran, T. T. Wang, S. Ebadi, H. Bernien, M. Greiner, V. Vuletić, H. Pichler, and M. D. Lukin, Parallel Implementation of High-Fidelity Multiqubit Gates with Neutral Atoms, *Phys. Rev. Lett.* **123**, 170503 (2019).
- [19] F. Sauvage and F. Mintert, Optimal Control of Families of Quantum Gates, *Phys. Rev. Lett.* **129**, 050507 (2022).
- [20] C. P. Koch, U. Boscain, T. Calarco, G. Dirr, S. Filipp, S. J. Glaser, R. Kosloff, S. Montangero, T. Schulte-Herbrüggen, D. Sugny, and F. K. Wilhelm, Quantum optimal control in quantum technologies. Strategic report on current status, visions and goals for research in Europe, *EPJ Quantum Technol.* **9**, 19 (2022).
- [21] M. Kalinowski, N. Maskara, and M. D. Lukin, Non-Abelian Floquet Spin Liquids in a Digital Rydberg Simulator, *Phys. Rev. X* **13**, 031008 (2023).
- [22] C. Dłaska, K. Ender, G. B. Mbeng, A. Kruckenhauser, W. Lechner, and R. van Bijnen, Quantum Optimization via Four-Body Rydberg Gates, *Phys. Rev. Lett.* **128**, 120503 (2022).
- [23] M. Morgado and S. Whitlock, Quantum simulation and computing with Rydberg-interacting qubits, *AVS Quantum Sci.* **3** (2021).
- [24] I. S. Madjarov, J. P. Covey, A. L. Shaw, J. Choi, A. Kale, A. Cooper, H. Pichler, V. Schkolnik, J. R. Williams, and M. Endres, High-fidelity entanglement and detection of alkaline-earth Rydberg atoms, *Nat. Phys.* **16**, 857–861 (2020).
- [25] M. Peper, Y. Li, D. Y. Knapp, M. Bileska, S. Ma, G. Liu, P. Peng, B. Zhang, S. P. Horvath, A. P. Burgers, and J. D. Thompson, Spectroscopy and modeling of ^{171}Yb Rydberg states for high-fidelity two-qubit gates (2024), arXiv:2406.01482.
- [26] A. B. Magann, C. Arenz, M. D. Grace, T.-S. Ho, R. L. Kosut, J. R. McClean, H. A. Rabitz, and M. Sarovar, From Pulses to Circuits and Back Again: A Quantum Optimal Control Perspective on Variational Quantum Algorithms, *PRX Quantum* **2**, 010101 (2021).
- [27] A. Pagano, S. Weber, D. Jaschke, T. Pfau, F. Meinert, S. Montangero, and H. P. Büchler, Error budgeting for a controlled-phase gate with strontium-88 Rydberg atoms, *Phys. Rev. Res.* **4**, 033019 (2022).
- [28] M. Mohan, R. de Keijzer, and S. Kokkelmans, Robust control and optimal Rydberg states for neutral atom two-qubit gates, *Phys. Rev. Res.* **5**, 033052 (2023).
- [29] C. Fromonteil, R. Tricarico, F. Cesa, and H. Pichler, Hamilton-Jacobi-Bellman equations for Rydberg-blockade processes, *Phys. Rev. Res.* **6**, 033333 (2024).
- [30] M. Saffman, I. I. Beterov, A. Dalal, E. J. Páez, and B. C. Sanders, Symmetric Rydberg controlled- Z gates with adiabatic pulses, *Phys. Rev. A* **101**, 062309 (2020).
- [31] D. Jaksch, J. I. Cirac, P. Zoller, S. L. Rolston, R. Côté, and M. D. Lukin, Fast Quantum Gates for Neutral Atoms, *Phys. Rev. Lett.* **85**, 2208 (2000).
- [32] N. Khaneja, T. Reiss, C. Kehlet, T. Schulte-Herbrüggen, and S. J. Glaser, Optimal control of coupled spin dynamics: design of NMR pulse sequences by gradient ascent algorithms, *J. Magn. Reson.* **172**, 296 (2005).
- [33] J. Tilly, H. Chen, S. Cao, D. Picozzi, K. Setia, Y. Li, E. Grant, L. Wossnig, I. Rungger, G. H. Booth, and J. Tennyson, The Variational Quantum Eigensolver: A review of methods and best practices, *Phys. Rep.* **986**, 1–128 (2022).
- [34] K. Hornik, Approximation capabilities of multilayer feed-forward networks, *Neural Netw.* **4**, 251 (1991).
- [35] L. H. Pedersen, N. M. Møller, and K. Mølmer, Fidelity of quantum operations, *Phys. Lett. A* **367**, 47 (2007).
- [36] D. P. Kingma and J. Ba, Adam: A Method for Stochastic Optimization, in *Proc. 3rd Int. Conf. Learn. Represent. 2018* (San Diego, 2015).
- [37] R. T. Q. Chen, Y. Rubanova, J. Bettencourt, and D. K. Duvenaud, Neural Ordinary Differential Equations, in *Adv. Neural. Inf. Process. Syst.*, Vol. 31 (Curran Associates, Inc., 2018).
- [38] D. E. Rumelhart, G. E. Hinton, and R. J. Williams, Learning representations by back-propagating errors, *Nature* **323**, 533 (1986).
- [39] A. G. Baydin, B. A. Pearlmutter, A. A. Radul, and J. M. Siskind, Automatic Differentiation in Machine Learning: a Survey, *J. Mach. Learn. Res.* **18**, 1 (2018).
- [40] N. Lacroix, C. Hellings, C. K. Andersen, A. Di Paolo, A. Remm, S. Lazar, S. Krinner, G. J. Norris, M. Gabureac, J. Heinsoo, *et al.*, Improving the Performance of Deep Quantum Optimization Algorithms with Continuous Gate Sets, *PRX Quantum* **1**, 020304 (2020).
- [41] R. De Keijzer, J. Snijders, A. Carvalho, and S. Kokkelmans, Pulse family optimization for parametrized quantum gates using spectral clustering, *Acad. Quantum* **1** (2024).
- [42] M. Mohan, J. de Hond, and S. Kokkelmans, Additional data for publication (2024).
- [43] L. S. Theis, F. Motzoi, F. K. Wilhelm, and M. Saffman, High-fidelity Rydberg-blockade entangling gate using shaped, analytic pulses, *Phys. Rev. A* **94**, 032306 (2016).
- [44] C. Fromonteil, D. Bluvstein, and H. Pichler, Protocols for Rydberg Entangling Gates Featuring Robustness against Quasistatic Errors, *PRX Quantum* **4**, 020335 (2023).
- [45] N. Bjorck, C. P. Gomes, B. Selman, and K. Q. Weinberger, Understanding Batch Normalization, in *Adv.*

- Neural. Inf. Process. Syst.*, Vol. 31 (Curran Associates, Inc., 2018).
- [46] F. N. Iandola, M. W. Moskewicz, K. Ashraf, and K. Keutzer, FireCaffe: Near-Linear Acceleration of Deep Neural Network Training on Compute Clusters, in *Proc. IEEE Comput. Soc. Conf. Comput. Vis. Pattern Recognit.* (2016).
- [47] P. Doria, T. Calarco, and S. Montangero, Optimal Control Technique for Many-Body Quantum Dynamics, *Phys. Rev. Lett.* **106**, 190501 (2011).
- [48] H.-J. Liao, J.-G. Liu, L. Wang, and T. Xiang, Differentiable Programming Tensor Networks, *Phys. Rev. X* **9**, 031041 (2019).
- [49] A. Paszke, S. Gross, F. Massa, A. Lerer, J. Bradbury, G. Chanan, T. Killeen, Z. Lin, N. Gimeshein, L. Antiga, *et al.*, PyTorch: An Imperative Style, High-Performance Deep Learning Library, in *Adv. Neural. Inf. Process. Syst.*, Vol. 32 (Curran Associates, Inc., 2019).
- [50] R. T. Q. Chen, PyTorch implementation of differentiable ODE solvers, GitHub repository (2018), <https://github.com/rtqichen/torchdiffeq>.
- [51] B. Hanin, Which Neural Net Architectures Give Rise to Exploding and Vanishing Gradients?, in *Adv. Neural. Inf. Process. Syst.*, Vol. 31 (Curran Associates, Inc., 2018).
- [52] I. S. Madjarov, *Entangling, Controlling, and Detecting Individual Strontium Atoms in Optical Tweezer Arrays*, Ph.D. thesis, California Institute of Technology (2021).
- [53] C. Sheng, X. He, P. Xu, R. Guo, K. Wang, Z. Xiong, M. Liu, J. Wang, and M. Zhan, High-Fidelity Single-Qubit Gates on Neutral Atoms in a Two-Dimensional Magic-Intensity Optical Dipole Trap Array, *Phys. Rev. Lett.* **121**, 240501 (2018).
- [54] A. D. Hill, M. J. Hodson, N. Didier, and M. J. Reagor, Realization of arbitrary doubly-controlled quantum phase gates (2021), arXiv:2108.01652 [quant-ph].